

# Genesis and magma fertility of gold associated high-K granites: LA-ICP-MS zircon trace element and REEs constraint from Bakoshi–Gadanya granites in NW Nigeria

Safiyau Muhammad Elatikpo<sup>1,2</sup> · Huan Li<sup>1</sup> · Yuanlin Chen<sup>1</sup> · Hafizullah Abba Ahmed<sup>3</sup>

Received: 2 December 2021 / Revised: 25 January 2022 / Accepted: 25 January 2022 / Published online: 21 March 2022

© The Author(s), under exclusive licence to Science Press and Institute of Geochemistry, CAS and Springer-Verlag GmbH Germany, part of Springer Nature 2022

**Abstract** High-K granites dominate the rock units in the Bakoshi and Gadanya areas located in the northwestern Nigerian subshield, part of the Trans-Saharan Belt, West Africa. In this contribution, the LA-ICP-MS zircon trace element revealed the fertility of magma responsible for the high-K granites that hosts the Bakoshi–Gadanya gold mineralization. Two likely metallogenic granites types are 1) Gadanya alkali granite, with high Ce<sup>4+</sup>/Ce<sup>3+</sup> (mean 1485) and limited range of Eu anomalies may likely be associated with the gold mineralization, and 2) Bakoshi porphyritic granite, Jaulere biotite granite, Shanono coarse-grained granite, and Yettiti granite, all have low Ce<sup>4+</sup>/Ce<sup>3+</sup> ratios (mean < 100, except second Bakoshi granite D2-1) with wider ranges of Eu/Eu\* values, thus are considered reduced granites. These reduced granites have oxygen fugacity values and Eu anomalies comparable to reduced granites associated with tin belts in Myanmar and Zaaiplaats granites in Bushveld Complex, South Africa. Ti-in-Zircon thermometric study revealed two thermal regimes during the crystallization of the Bakoshi–Gadanya granites: the high temperature (746–724 °C): Shanono coarse-grained granite, Bakoshi granite D2-1, and Jaulere biotite granite; and relatively low temperature (705–653 °C):

Bakoshi porphyritic granite D1-1, Yettiti medium-grained granite, and Gadanya alkali granite. Zircon trace elements including U, Yb, Y, Nb, and Sc ratios constraint the magma source of Bakoshi–Gadanya granites to an enriched mantle metasomatized during the subduction process before its melting. Except for Gadanya alkali granite, fractionation of titanite and apatite dominate the magma evolution with limited amphibole fractionation. Melt that crystallized Gadanya alkali granite is rather saturated in zircon without accessory titanite or apatite.

**Keywords** Bakoshi–Gadanya area · Zircon trace element · Europium anomalies · Gold mineralization · Oxygen fugacity · Cerium ratio

## 1 Introduction

Zircon mineral is versatile in many aspects due to its resistance to post-crystallization alteration and ability to store information relating to chemical elements since crystallization time (Ballard et al. 2002; Trail et al. 2012; Jiang et al. 2019, 2020). Its applications range from geochronological investigations, melt and fluid sources tracer through Hf-isotopes in zircon, and geothermometers (Harrison et al. 2005; Kemp et al. 2010; Bouvier et al. 2011; Watson and Harrison 1983; Boehnke et al. 2013). As a typical accessory phase in most rocks, zircon is the major reservoir for U, Th, Hf, and HREE and also aid incorporation of other elements such as Y, Nb, and Ta due to its unique crystal structure (Bea 1996; Belousova et al. 2002; Corfu et al. 2003; Linch and Hanchar 2003).

Europium and cerium in zircon are used to ascertain the redox state of magma and the extent of fractional

✉ Huan Li  
lihuan@csu.edu.cn

<sup>1</sup> Key Laboratory of Metallogenesis Prediction of Nonferrous Metals and Geological Environment Monitoring, Ministry of Education, School of Geosciences and Info-Physics, Central South University, Changsha 410083, China

<sup>2</sup> Department of Geology, Ahmadu Bello University, Zaria, Nigeria

<sup>3</sup> Department of Geology, Modibbo Adama University of Technology, P.M.B. 2076, Yola, Nigeria

crystallization which can proffer valuable information relating to ore element concentration, source rock, magnetic susceptibility, and the type of associated ore deposit (Blevin and Chappell 1995, 1992; Blevin et al. 1996; Chappell and White 2001; Kemp 2005). For example, Au, Cu, and Mo mineralization usually are tied to oxidized granites, while Sn, Wo, and Ta mineralization are associated with reduced granites (Kemp 2005; Sun et al. 2013; Cheng et al. 2018; Lee et al. 2021). A distinction is usually drawn using Fayalite-Magnetite-Quartz (FMQ) oxygen buffer line to separate granite magmas that are oxidized and plot above the FMQ (usually crystallize magnetite) from those reduced granitic magmas with relatively lower oxygen fugacity compared with FMQ which crystallize ilmenite (Blevin and Chappell 1995; Ishihara 1977; Kemp 2005). Thus, granitic rocks associated with gold are magnetite-bearing, oxidized, and display pronounced aeromagnetic signature, while those with no genetic association but host gold are ilmenite-bearing, are reduced, and show less aeromagnetic signatures. Cerium and Eu usage as oxy-barometer is gaining acceptance by many researchers in finding answers to magma redox state, where higher  $\text{Ce}^{+4}/\text{Ce}^{+3}$  implies oxidized magma condition whereas lower Eu anomaly constraints the reducing environment (Ballard et al. 2002; Trail et al. 2012; Smythe and Brenan 2016; Jiang et al. 2019; Girei et al. 2020; Lee et al. 2021). Although some researchers (e.g. Hoskin and Schaltegger 2003) envisage caution when applying this oxy-barometer due to plagioclase fractionation or co-crystallization with zircon as it would elevate the anomaly in Eu, which may be confused for change in the redox state of magma or fluid. However, the work of Trail et al. (2012) has shown that  $\text{Eu}^{2+}$  and  $\text{Ce}^{4+}$  can coexist in silicate melt and can be used as proxies for the redox state of magma saturated with zircons. Therefore, feldspar crystallization, whether during or before zircon formation, is not a requirement for the observed Eu anomaly in zircon, somewhat, the oxygen fugacity and Eu anomaly of the magma.

The Bakoshi-Gadanya (BAG) area is known for its high-K igneous rocks (Elatikpo et al. 2021). In recent times, this category of igneous rock has attracted the attention of geoscientists from both the academics and in the exploration industries about their petrogenesis, potentials, and their close association with gold mineralization (Müller and Groves 2019). Although some workers (e.g. Asaah et al. 2015, and references therein) conversed for an all-inclusive granitic rock with no preferences for a particular compositional range as capable of association with gold. High-K calc-alkali to alkali-calcic granitic rocks is associated with the newly discovered gold mineralization in the BAG area. At present, there is no documented evidence either through geochemical or isotope systematics to suggest a metamorphic or magmatic origin of the fluid

source(s) responsible for the BAG gold mineralization. The possibility of a magmatic fluid source contribution to the associated gold mineralization should not be quickly overruled. Recently, a regional ore source fluid was proposed linking some gold mineralization in the Pan-African terrane of western Africa to granitic host rocks (e.g. Asaah et al. 2015; Ouattara et al. 2020). The present investigation tests the likely potential of the BAG high-K granitic rocks by assessing their magma fertility concerning the associated gold mineralizing fluid.

The present contribution reports the results of Laser Ablation Inductively Coupled Plasma Mass Spectrometry (LA-ICP-MS) study of zircon trace element and REE precipitation during magmatic crystallization stage, based on the example of the gold-hosted high-K BAG granites in northwestern Nigeria. The ultimate goals are (1) to document the magma source(s) and the geodynamic setting from which the BAG granite form and (2) to assess the magma fertility of the granites concerning the associated gold mineralization.

## 2 Geological background

### 2.1 Regional geology

The Nigerian shield is an extended component of the Trans-Saharan Orogenic Belt (TSOB) that runs from Hoggar in Algeria down to the Atlantic Ocean. This belt has a trans-continental counterpart as Borborema province in NE Brazil (Caby 2003; De Wit et al. 2008; Liégeois 2019). The TSOB is situated between the West African Craton (WAC), the Congo Craton (CC), and the Saharan metacraton (SmC), which have suffered multiple orogenies, including the recent Pan-African orogeny (Ajibade and Wright 1989; Brahimi et al. 2018; Liégeois 2019; Elatikpo et al. 2021). Terranes in the TSOB are primarily divided along mega shear zones such as the Adrar, Iskel, Ounane, and Raghane shear zones in Tuareg Shield (covering countries like Mali, Algeria, and Niger) and the Anka-Zungeru and Kalangai-Ifewara shear zones in the southern segment (the Nigerian Shield) (Ajibade and Wright 1989; Brahimi et al. 2018; Liégeois 2019). The shear zones trend majorly in N–S and NE–SW directions. Both Archean and Proterozoic rocks have been reported in TSOB (Ogezi 1977; Dada et al. 1989; Bruguier et al. 1994; Kröner et al. 2001; Béchiri et al. 2011, 2018; Liégeois 2019 and references therein).

The Nigerian shield—the southern prolongation of TSOB, is recognized as two subshields (Fig. 1a) which differs in rock ages, lithological units, and mineralization potentials (Ananaba and Ajakaiye 1987; Woakes et al. 1987; Ferré et al. 1996; Bute et al. 2020a): the west

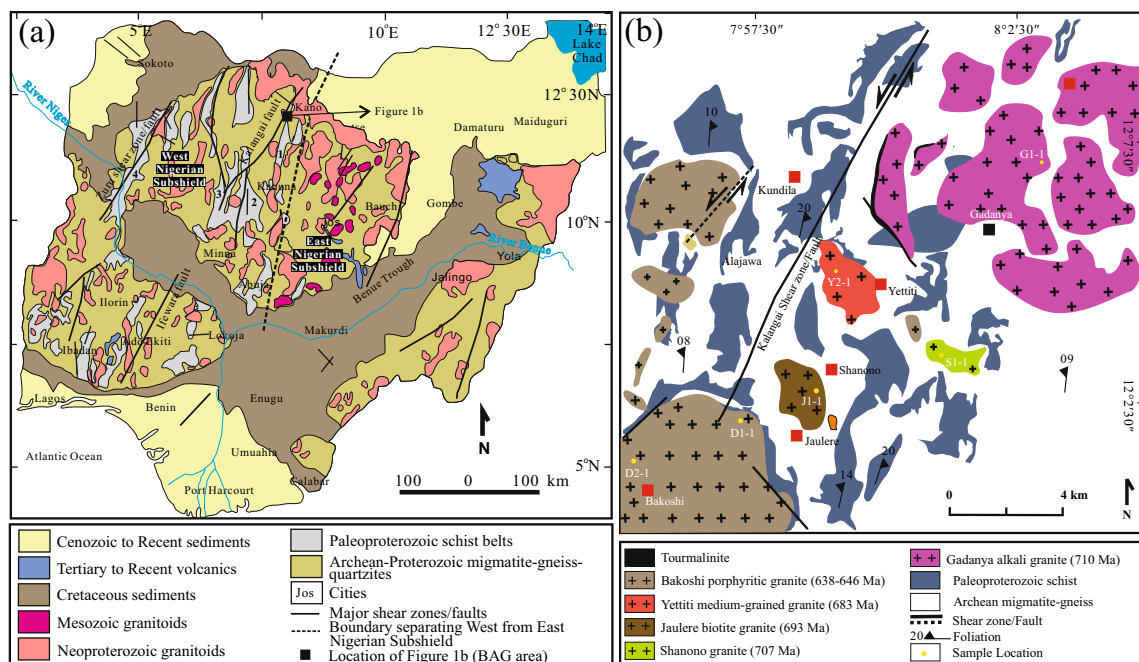


**Fig. 1** **a** Simplified geological map of Nigeria (merged from Dada 1998; Goodenough et al. 2014; Elatikpo et al. 2021), location of **b** is represented by the black filled rectangle; 1–Malumfashi Schist Belt, 2–Kushaka Schist Belt, 3–Birnin Gwari Schist Belt, 4–Zuru Schist Belt; **b** Geological map of Bakoshi and Gadanya area (merged from Elatikpo et al. 2021)

Nigerian subshield (WNS) have Archean to Paleoproterozoic rocks including gneisses and schists that formed during greenschist to amphibolite-facies metamorphism; they comprise gold and banded-iron metallogenic provinces. The east Nigerian subshield (ENS) is noted for its Eburnean rocks of granulite-facies metamorphism and constitutes Nigeria's tin and uranium metallogenic provinces. In these two subshields are also granitoids of Neoproterozoic ages formed during the Pan-African tectono-thermal events, locally called 'Older Granites.' The granitoids range from metaluminous variety (mostly the granodiorite, diorite, and syenite) to peraluminous (mostly granites) and range from magnesian to ferroan in composition, with I-, S-, or A-type granite affinity (Goodenough et al. 2014; Bute et al. 2020b; Elatikpo et al. 2021). These granitoids are reported to be related to the subduction on the margin of the WAC (Danbatta 1999; Goodenough et al. 2014) or other subductions on the margins of crustal blocks in the Nigerian Shield (e.g., Adetunji et al. 2018; Elatikpo et al. 2021).

## 2.2 Local geology and gold mineralization

The BAG is part of the WNS (Fig. 1b) in TSOB. The area is underlined by rocks of Archean gneisses, Paleoproterozoic metasedimentary schists, and quartzite, which are intruded by Cryogenian granites and aplites with minor pegmatites (Elatikpo et al. 2021). Tourmalinite is a later

boron fluid metasomatized rock with limited coverage and may likely represent the youngest unit in this area (age unknown). The gneisses are mostly of banded and granitic variety and occupy most parts of the BAG area. On the other hand, metasedimentary rocks are sparsely distributed with orientation controlled mainly by the dominant Pan-African structural North- to NE-trends. They are dominantly mica schists, phyllite, and quartzites.

Only recently, Elatikpo et al. (2021), using whole-rock geochemical and U-Pb on zircon isotopic studies of the high-K BAG granites, asserted that the granites are synkinematic to second major syn-metamorphic deformation with calc-alkalic to alkali-calcic affinity. The authors put the magmatic activities to have spanned c. 70 million years (710–638 Ma) and linked their parental magmas to metasomatized mantle lithosphere and asthenospheric mantle. The authors also grouped the granites into two geochemical types, namely: 1) the calc-alkalic type including the Bakoshi porphyritic granite (D1-1: 638 Ma; D2-1: 646 Ma), Jaulere biotite granite (J1-1; 693 Ma), Shanono medium- to coarse-grained granite (S1-1; 707 Ma), and the Yettiti medium-grained granite (Y2-1; 683 Ma), and 2) the Gadanya alkali granite (G1-1; 710 Ma) which constitute the alkali-calcic type. These granites are slightly peraluminous, ferroan, and are akin to A-type granites. For detailed geochemical, geochronological, and isotopic information relating to the BAG granites, the reader is referred to the work of Elatikpo et al. (2021).

The first documented report of gold occurrence in the BAG area was the work of Elatikpo (2016) and later Sani et al. (2017), Elatikpo et al. (2018), and Anthony et al. (2020). Their works centred on the style of occurrence, local structural control, and metallurgy of the gold (Anthony et al. 2020; Sani et al. 2017). These authors reported gold mineralization styles as vein type, stockwork, and wall-rock dissemination. Issues that border genesis, source of ore fluid, and timing of gold mineralization are yet to be investigated or reported in this new goldfield. These earlier workers indirectly linked the gold mineralization to a shared regional fluid source, transported along the major transcurrent Kalangai fault which traversed the area. The precipitation of gold and other ore minerals was envisaged to be in the second and/or third-order conjugate faults systems (e.g. Sani et al. 2017), thus, conversing a structural control as the mechanism of their deposition.

### 3 Analytical method

Six fresh granite samples collected from the six granitic phases in the Bakoshi–Gadanya area were crushed and ground to extract the zircon grains. These zircon grains were separated from the bulk minerals through density and magnetic separation techniques, and the clean grains were then mounted in an epoxy resin and, after that, polished. Fractures and mineral or fluid inclusions were avoided using cathodoluminescence (CL) images of the zircon grains taken using a scanning electron microscope, fitted with energy dispersive spectroscopy (EDS). This was in addition to transmitted and reflected light images of the zircons before the laser spots were rightfully selected for investigation of trace and rare earth elements.

*In-situ* zircon trace elements and REEs were determined at Beijing Geo-Analysis Co. Ltd China, using Laser Ablation Inductively Coupled Plasma Mass Spectrometry (LA-ICP-MS). Ion-signal intensities were acquired using an excimer laser ablation system fitted with an Agilent 7500a ICP-MS, and the laser energy and frequency used were 70 mJ and 8 Hz, respectively. Helium and argon were used as the carrier and make-up gases, respectively, mixed with nitrogen during the procedure. The chosen Laser beam diameter was 32  $\mu\text{m}$  for most grains except for a few grain with a smaller width, in which case, a 24  $\mu\text{m}$  spot diameter was applied on such zircons. Background and data acquisition intervals of  $\sim 20$ –30 s (gas blank) and a 40 s, respectively, were applied on the chosen zircon spots for each of the analyses. The calibration was against NIST 610 combined with Zr as internal standard, processed using Iolite v3.7 software. Reference material was analyzed (see Table S4 in Electronic Supplementary Material) between 10 unknown analyses to correct for time-dependent drift of

sensitivity and mass discrimination. Analytical results obtained were processed, and plots were constructed using Grapher 13 software.

## 4 Results

Trace elements and rare earth elements (REE) results used in this study derived from 94 zircons from the Bakoshi–Gadanya granites (30 grains from two Bakoshi porphyritic granites; 17 grains from Shanono coarse-grained granite; 12 grains from Yettiti medium-grained granite; 22 grains from Gadanya alkali granite; and 13 grains from Jaulere biotite granite). The results are listed in Electronic Supplementary Material Table S1 and presented in Figs. 2, 3, 4, 5, 6 and 7.

Crystallization temperatures were determined using the titanium concentration in zircon (Watson et al. 2006; Fu et al. 2008). Considering that zircon coexists with Ti-bearing phases, e.g., titanite, in some samples from the BAG granites (Elatikpo et al. 2021), Titanium activity ( $a_{\text{TiO}_2}$ ) was set at 0.8 with the belief that Ti concentration could have been high during the melt evolution. Due to silicic compositions of BAG granites (Elatikpo et al. 2021), silica activity ( $a_{\text{SiO}_2}$ ) was set to one. Parameters such as temperature, oxygen fugacity ( $f\text{O}_2$ ), Eu- and Ce-anomalies, and  $\text{Ce}^{4+}/\text{Ce}^{3+}$  ratios were calculated from the zircon trace elements and REE data. These parameters are given in Electronic Supplementary Material Table S2 and presented in Figs. 5, 6 and 8. Chondrite-normalized REE values of zircons are listed in Electronic Supplementary Material Table S3. Cathodoluminescence (CL) and reflected light (RF) images of the investigated zircons are presented in Fig. 9.

### 4.1 Trace elements and REEs in zircons

Zircons from the BAG high-K granites are rich in Hf, U, and Y and heavy REE over light REE (see Table S1). The calc-alkaline granite samples (D1-1, D2-1, J1-1, S1-1, and Y2-1) have higher but variable Hf concentrations (18,140–8350 ppm) in their zircons. Zircons from Gadanya alkali granite have lower and consistent Hf concentrations around 11870–8300 ppm.

In most samples, chondrite-normalized REE patterns of zircons are similar, though with varying degrees of REE enrichment (Fig. 2). This also applies to trace element patterns (Fig. 2g). They are characterized by rising slopes from the light REE to heavy REE, with Ce enrichment and pronounced Eu depletion (Fig. 2)—a characteristic of unaltered zircon (Hoskin and Schaltegger 2003). A close inspection of the patterns revealed an abrupt rise in heavy REE from Gd to Lu with variable  $(\text{Yb}/\text{Sm})_N$  ratios in all the

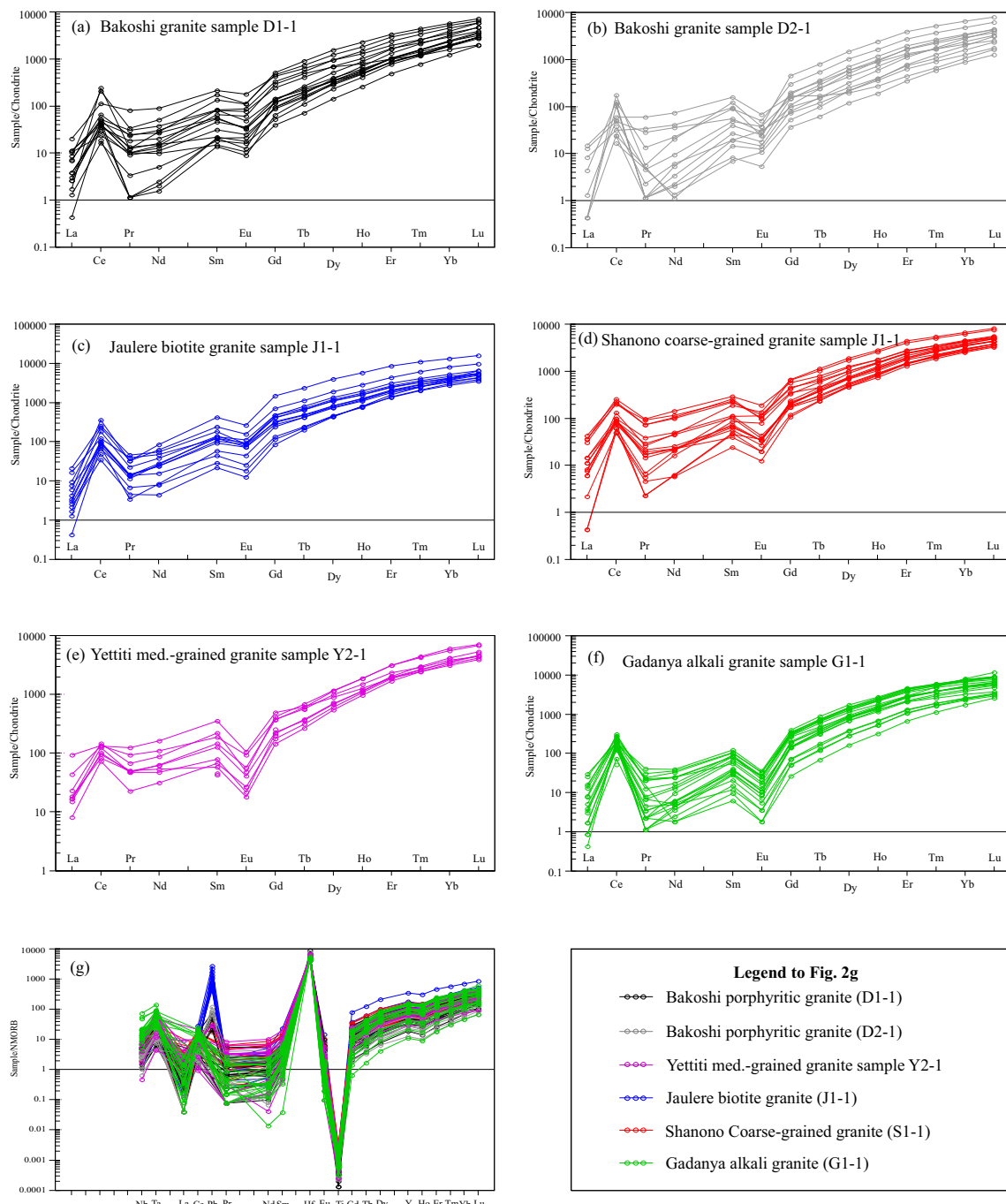


**Fig. 2** Distribution patterns of trace elements and REE in zircons from BAG granites. Note the consistent enrichment in heavy REE over the light REE in all the zircons from the different granitic phases. Normalization values are taken from Anders and Grevesse (1989) and Sun and McDonough (1989) for REE and trace elements, respectively

zircons populations (Fig. 2 and Fig. S1; see Table S3 for  $\text{Yb}_N/\text{Sm}_N$  ratios). The  $(\text{Yb}/\text{Sm})_N$  ratios have been used to evaluate heavy REE enrichment in zircons (Belousova et al. 2002). These ratios are low and variable across the quartiles in zircons from the calc-alkalic BAG granites: Bakoshi granite (mean D1-1: 72, D2-1: 95), Jaulere granite (mean 54), Shanono granite (mean 48), and Yettiti granite

(mean 76). However, variability in  $(\text{Yb}/\text{Sm})_N$  ratios are less in zircons from the alkali-calcic Gadanya granite (52 to 281, mean 127) with a greater population centred around 90–200 except for an outlier G1-1-15. The high but less variable  $(\text{Yb}/\text{Sm})_N$  ratios in zircons from Gadanya alkali granite justify their higher contents of heavy REE (Table S1).

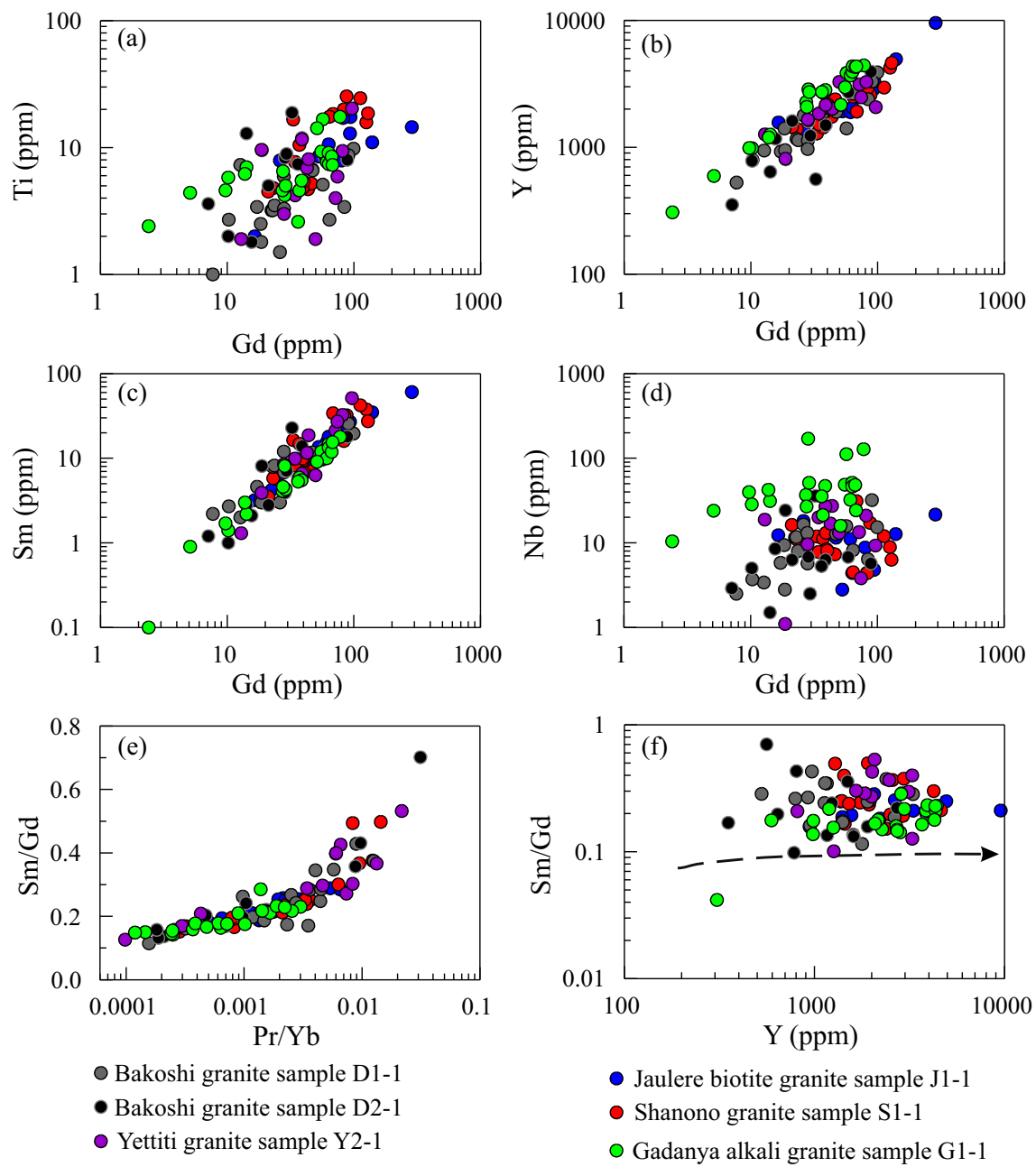


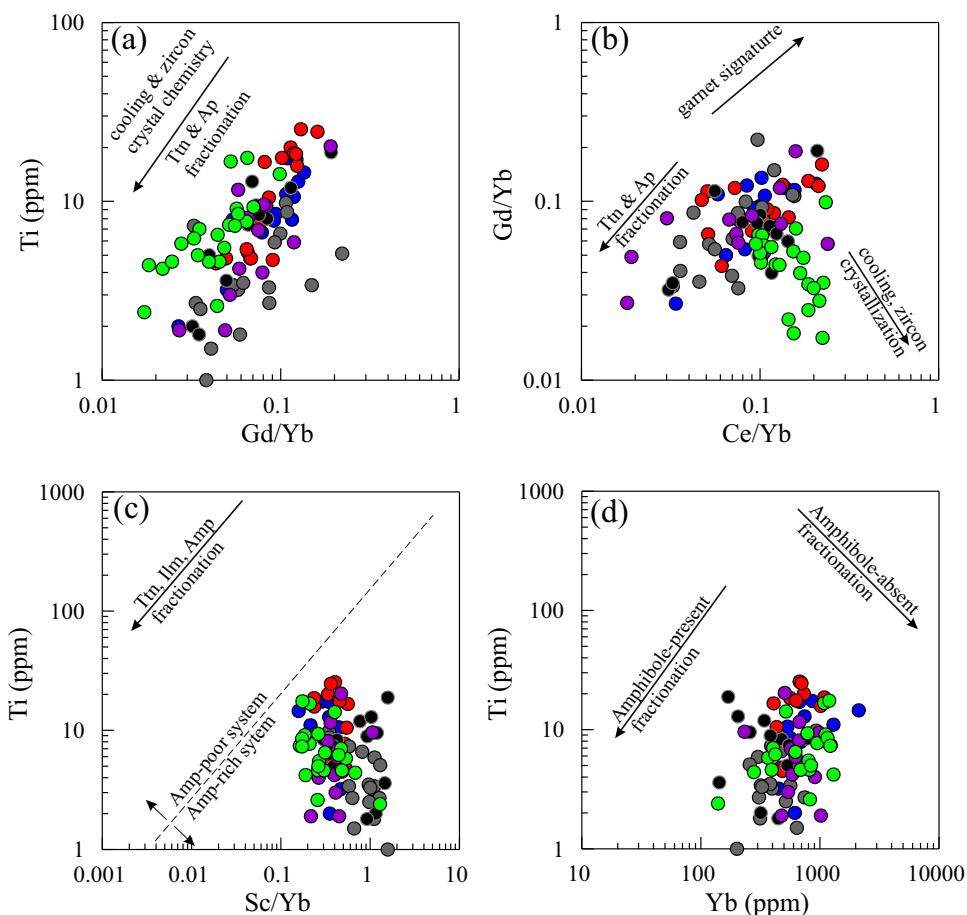
**Fig. 3** Correlation diagrams of selected trace elements (Ti, Y, Sm, Gd, and Nb) and REE ratios showing covariation of HFSE and REE in Bakoshi–Gadanya granites **a** Ti versus Gd; **b** Y versus Gd; **c** Sm versus Gd; **d** Nb versus Gd; **e** Sm/Gd versus Pr/Yb; and **f** Sm/Gd versus Y, the dashed line represent fractionation trend

#### 4.2 Ti in zircon temperature

The choice of Ti-in-Zircon thermometry as applied in this study comes from the fact that Ti can be incorporated into phases like titanite, ilmenite, and rutile; and can also substitute for Si in zircon (Watson et al. 2006; Fu et al. 2008). Therefore, once the oxide activities (e.g.  $a_{\text{TiO}_2}$  and  $a_{\text{SiO}_2}$ ) are known and the older zircon populations, e.g., xenocrysts and antecrysts are excluded, Ti-in-Zircon can

provide an excellent crystallization temperature of zircon, and by extension, that of BAG granitic phases. Based on the mean Ti-in-Zircon temperature values, the BAG granites are grouped into two (Table S2; Fig. 5a). The first group have relatively lower mean values and comprise Bakoshi granite sample D1-1 (range = 562–735 °C, mean = 653 °C), Yettiti granite sample Y2-1 (range = 809–605 °C, mean = 693 °C) and Gadanya alkali granite sample G1-1 (range = 797–624 °C, mean = 705 °C). The

**Fig. 4** Binary diagrams showing cooling and phase fractionation in zircons from the BAG granitic phases (after Grimes et al. 2015) **a** Ti versus Gd/Yb; **b** Gd/Yb versus Ce/Yb; **c** Ti versus Sc/Yb; and **d** Ti versus Yb. Ap = apatite; Ilm = ilmenite; Ttn = titanite; Amp = amphibole. Symbols are the same as in Fig. 3



second group, however, have their mean values higher than those observed in the first group; this comprises the Bakoshi granite sample D2-1 (range = 799–600 °C, mean = 713 °C), Jaulere granite sample J1-1 (range = 790–607 °C, mean = 724 °C) and Shanono granite sample S1-1 (range = 831–668 °C, mean = 746 °C). From Fig. 5a, it can be seen that samples from Bakoshi granite D1-1 and Gadanya alkali granite show fairly consistent temperature values in 25th and beyond 75th percentiles. Temperature values in Gadanya and Yettiti granites vary less across the quartiles. Temperature values in sample D2-1 are variable in both 25th to 50th percentiles, similar to variable temperatures displayed in 50th to 75th percentiles in Jaulere granite. The Shanono granite displayed homogenous temperature values in the 25th percentiles.

#### 4.3 Ce<sup>4+</sup>/Ce<sup>3+</sup> and Eu anomalies

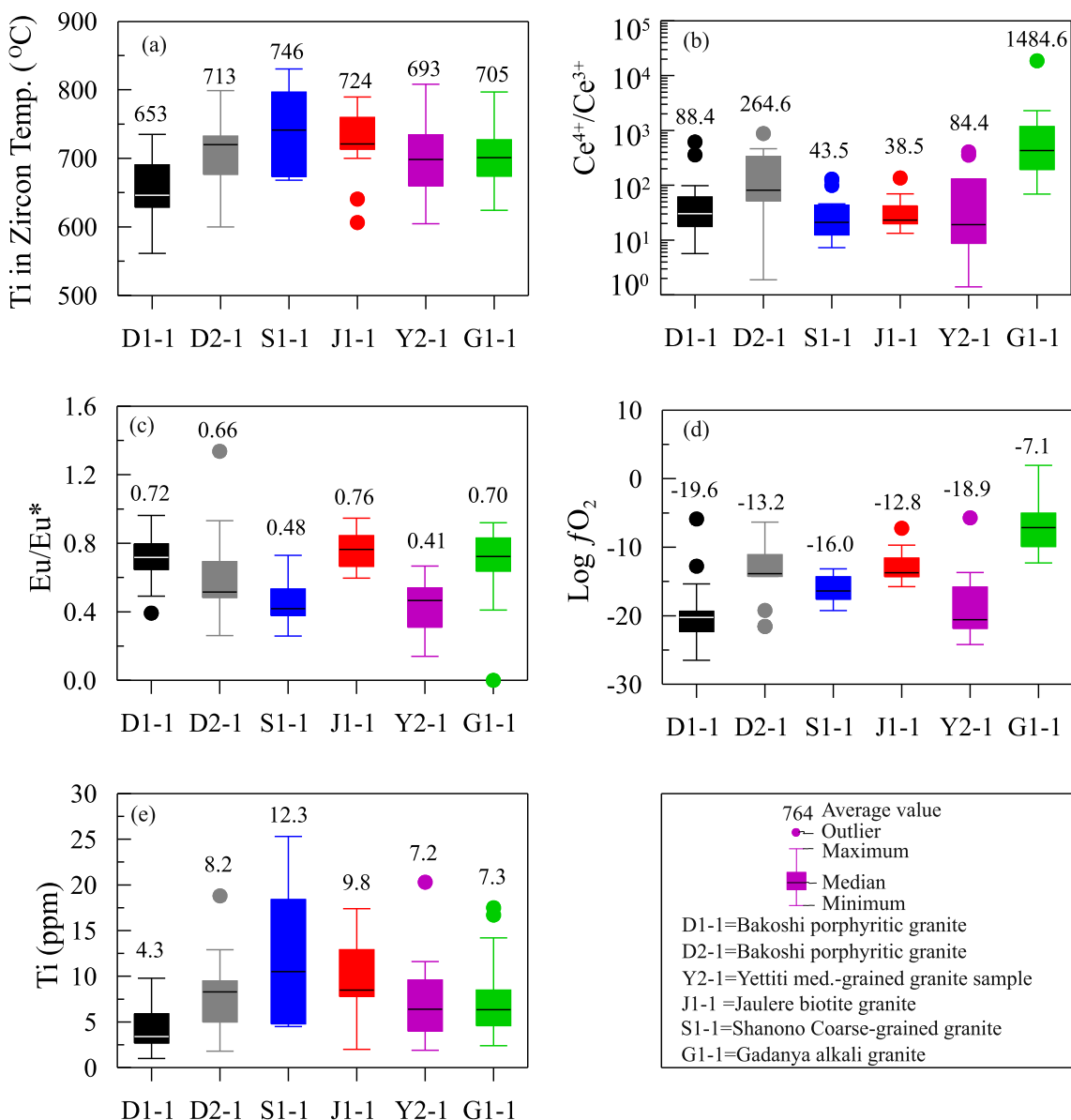
The Gadanya alkali granite has high zircon Ce<sup>4+</sup>/Ce<sup>3+</sup> ratios (range = 69–18,622, mean = 1485), although its mean Eu anomalies (range = 0.0–0.9, mean = 0.7) are comparable to those of Jaulere granite samples J1-1 (mean = 0.8) and Bakoshi granite (D1-1 = 0.7, D2-1 = 0.7) (Table S2, Fig. 5b–c). In comparison to Gadanya

alkali granite, the Jaulere and Bakoshi granites show lower zircon Ce<sup>4+</sup>/Ce<sup>3+</sup> ratios [(Jaulere: 13–136, mean = 39), (Bakoshi sample D1-1: 5.7–616, mean = 88; Bakoshi sample D2-1: 1.9–878, mean = 265)] (Table S2; Fig. 5b–c).

Yettiti granite have lower Ce<sup>4+</sup>/Ce<sup>3+</sup> ratios and Eu anomalies (Ce<sup>4+</sup>/Ce<sup>3+</sup> = 1.4–407, mean = 84; Eu/Eu\* = 0.3–0.7, mean = 0.5). Zircon Ce<sup>4+</sup>/Ce<sup>3+</sup> ratios in Shanono granite (Ce<sup>4+</sup>/Ce<sup>3+</sup> = 7.3–129, mean = 44) is comparable to that of Jaulere granite, but its Eu/Eu\* anomalies (0.3–0.7, mean = 0.5) equate that of Yettiti granite.

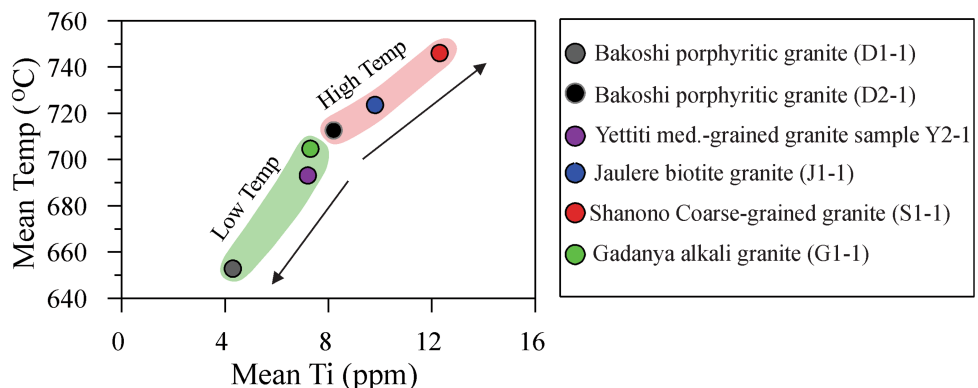
#### 4.4 Oxygen fugacity

Oxygen fugacity is exponentially high in the Gadanya alkali granite ( $\log O_2 = -12.3$  to 1.9, mean = −7.1) with its Fayalite-Magnetite-Quartz buffer ( $\Delta F_{MQ}$ ) determined at +4 to +21, mean = +9.5 (Table S2). Calculated oxygen fugacity in the Bakoshi granite is lower and below the FMQ buffer: sample D1-1 ( $\log O_2 = -26.5$  to −5.9, mean = −19.6),  $\Delta F_{MQ}$  (−8.3 to +10.6, mean = −1.5) and sample D2-1 ( $\log O_2 = -21.6$  to −6.4, mean = −13.2),  $\Delta F_{MQ}$  (−7.2 to +11, mean = +3.5). Jaulere and Shanono granites have values intermediate between the



**Fig. 5** Whisker and box statistical diagrams showing variability in **a** crystallization temperature; **b** Ce<sup>4+</sup>/Ce<sup>3+</sup> ratios; **c** Eu/Eu\* anomalies; **d** oxygen fugacity (log $f_{\text{O}_2}$ ) and; **(e)** Ti concentrations in zircons from the BAG granites

**Fig. 6** Mean Ti versus mean temperature plot showing two populations of magma crystallization temperatures of the BAG granites



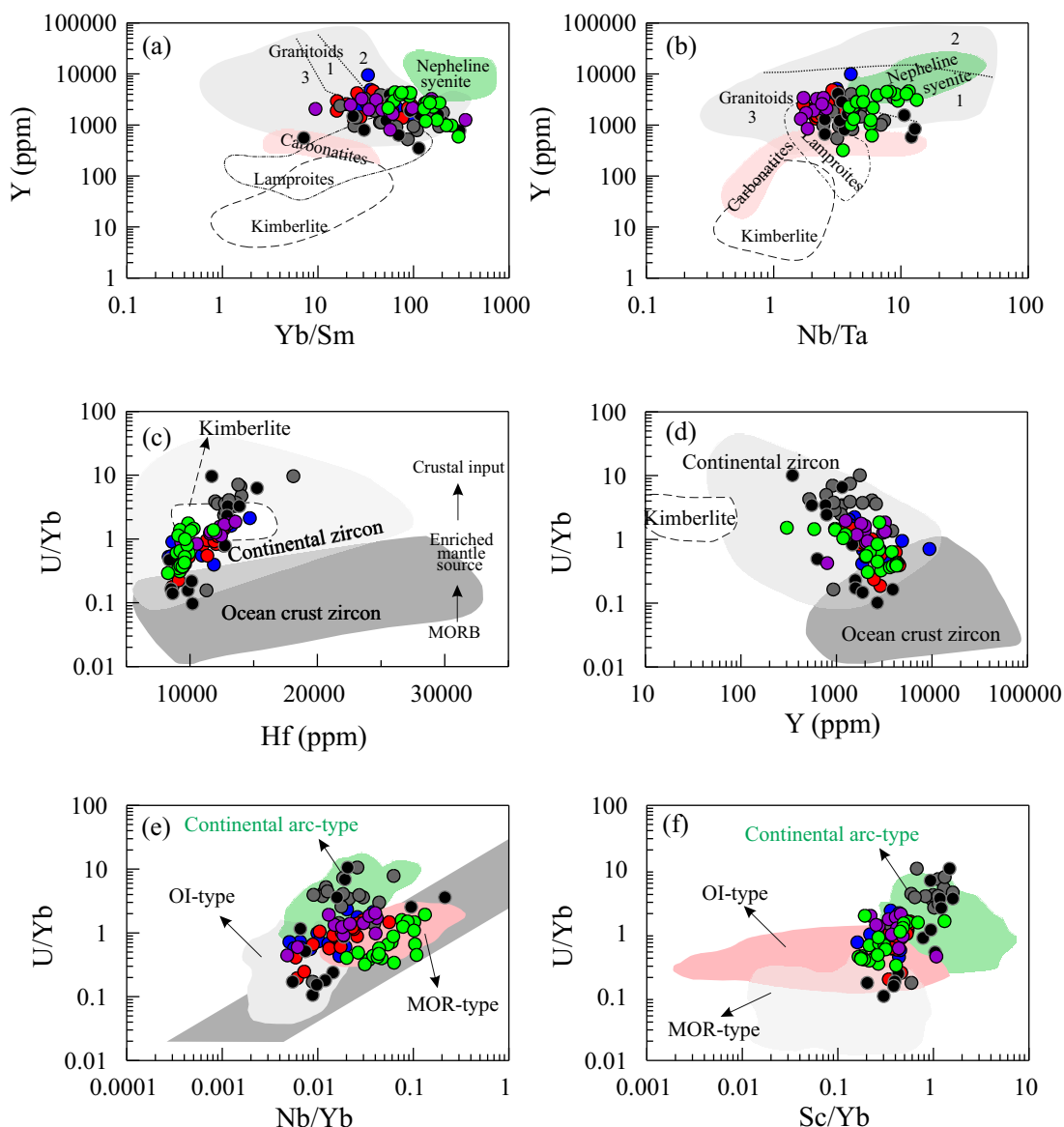


**Fig. 7** Discrimination diagrams showing the fields of granites type, enriched mantle, and asthenospheric sources occupied by zircons from BAG granites **a–b** Yb/Sm and Nb/Ta versus Y (after Belousova et al. 2002), 1—aplites and leucogranites, 2—granites, 3—granodiorites and tonalites; **c–d** U/Yb versus Hf and Y (after Grimes et al. 2007); **e–f** U/Yb versus Nb/Yb and Sc/Yb (after Grimes et al. 2015), gray color diagonal field represent mantle zircon array, MOR—mid-oceanic ridge, OI—oceanic island (asthenospheric melt). Uranium data are from Elatikpo et al. (2021, [www.tandfonline.com](http://www.tandfonline.com)). Symbols are the same as in Fig. 6

higher values in Gadanya alkali granite and lower values in the Bakoshi granite: Jaulere granite ( $\log fO_2 = -15.7$  to  $-7.2$ , mean =  $-12.8$  and  $\Delta FMO = -1.3$  to  $+7.2$ , mean =  $+1.6$ ), Shanono granite ( $\log fO_2 = -19.2$  to  $-13.1$ , mean =  $-16.0$  and  $\Delta FMO = -3.2$  to  $+4.0$ , mean =  $-0.2$ ).

## 5 Discussion

### 5.1 Trace element and REEs systematics

The fractionation or crystallization trend of mineral phases, e.g., accessory minerals, determined the contents of trace elements and REE in zircon (Schaltegger 2007) with preferential portioning of light rare earth elements (LREE) for apatite, monazite, and allanite against zircon in a typical magmatic-hydrothermal system (Krneta et al. 2017). In a detailed work using a large zircon chemical composition

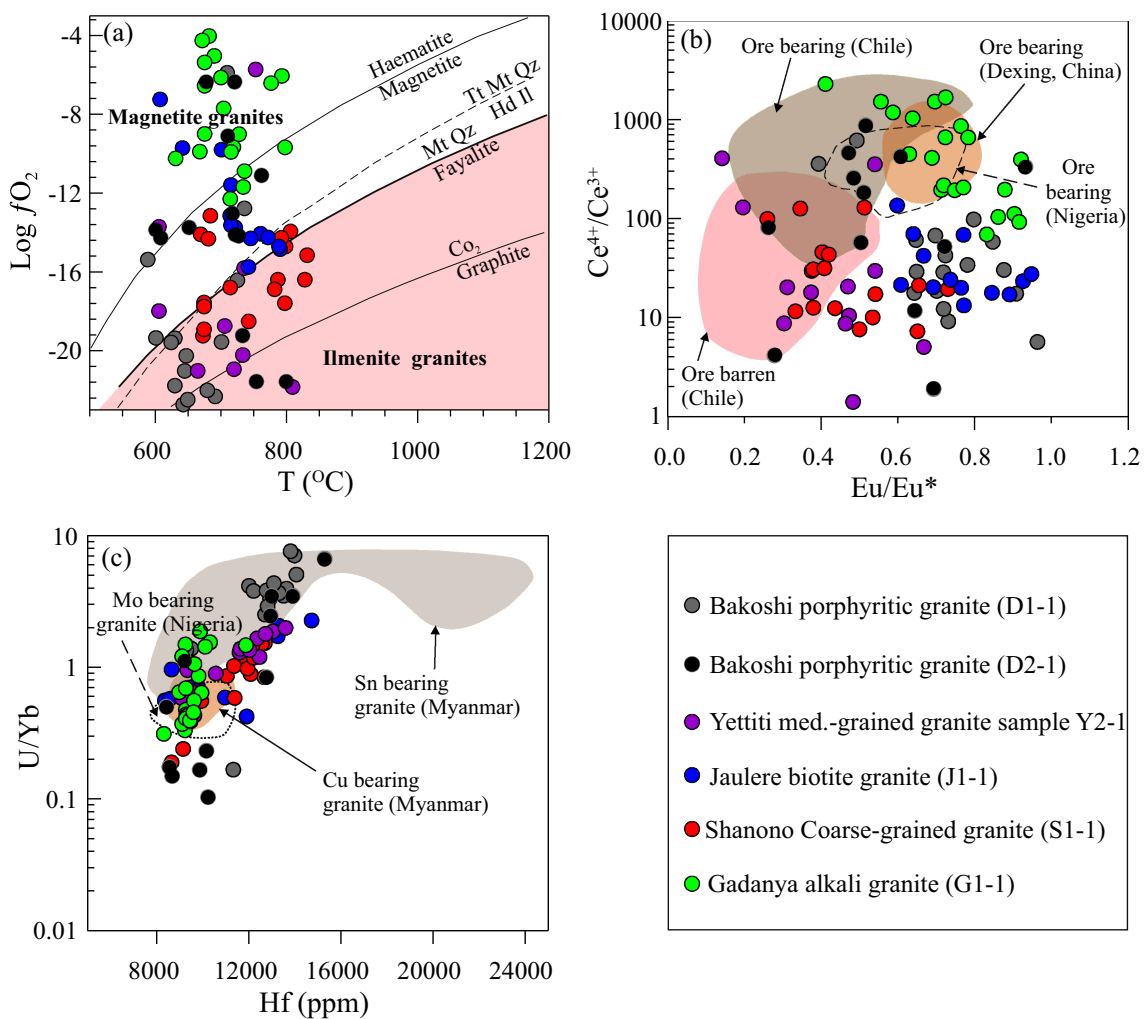


**Fig. 8** Binary diagrams illustrating the fertility of BAG granites' magma. **a** Temperature versus Log $f_{\text{O}_2}$  (after Ishihara 1977; Kemp 2005), white color in 'a' demarcate the oxidized granite boundary from the reduced granite represented in pink field/background, Hd = hedenbergite; Ilm = ilmenite; Mt = magnetite; Qz = quartz; Ttn = titanite; **b** Eu/Eu\* vs. Ce<sup>+4</sup>/Ce<sup>+3</sup> (after Zhang et al. 2020), ore-bearing and barren fields are given for comparison and were taken from Ballard et al. (2002), Zhang et al. (2020) and Girei et al. (2020). **c** Hf versus U/Yb, Mo, and Sn fields are given for comparison and were taken from Girei et al. (2020) and Gardiner et al. (2021), respectively

dataset, Zhong et al. (2018) established several pitfalls of magmatic versus hydrothermal zircon discrimination diagrams, e.g., (Sm/La)<sub>N</sub> vs La and Ce/Ce\* vs (Sm/La)<sub>N</sub> diagrams. The shreds of evidence given by the authors were germane and thus could not warrant their usage in this study to ascertain the magmatic from possibly hydrothermal zircon populations in the BAG granites. However, a combination of cathodoluminescence images of zircon that provide an excellent view of the zircon texture and trace element contents was adopted. Those zircons that are magmatic and autocryptic – with clear concentric zoning texture and a clear heavy REE-enrichment over light REE were chosen and discussed in this work.

Selected trace elements (Ti, Y, Sm, and Nb) were plotted against Gd to test for the fractionation in the BAG granites (Fig. 3). Clearly, these elements show good

correlations with Gd, indicating fractionation as one of the dominant mechanisms during the magma evolution of these granites. The patterns of REE, Y, and Ti contents in all the investigated zircons from the different granitic phases are similar and consistent with those of magmatic zircons, with enrichment in heavy REE over the light REE. In addition, the Eu anomalies are pronounced across the zircon populations. Also, a plot of differentiation index, Sm/Gd and Pr/Yb (e.g. Gardiner et al. 2021), have confirmed the fractionation mechanism as the zircons displayed a positive correlation (Fig. 3e–f). The covariation of REE and HFSE in Fig. 3 is a testimony that these elements in BAG zircons were not significantly disturbed (if they were) and can be taken to indicate magmatic signature.

Moreover, elements such as Sm, Gd, and Y, which are incompatible chemically, are used to measure fractionation

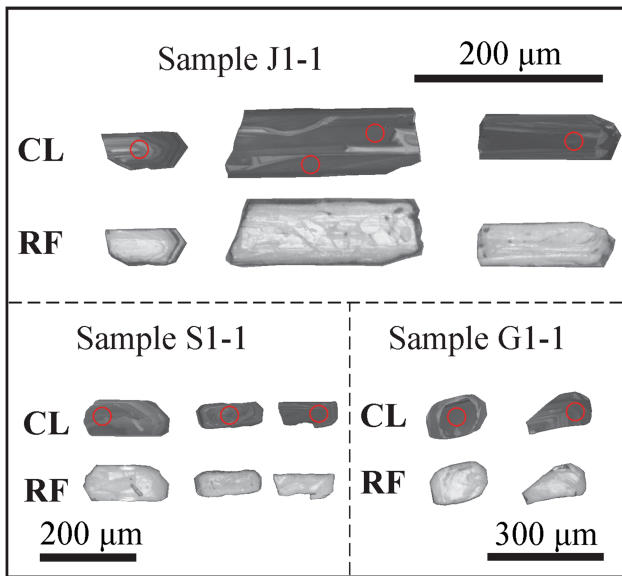


**Fig. 9** Cathodoluminescence (CL) and reflected light (RF) images of representative zircons extracted from the different granitic phases in the Bakoshi–Gadanya area. Note the texture typical of magmatic zircon

in felsic magmatism, such as BAG zircons (Belousova et al. 2002), with minimal variability in Sm/Gd ratios. In Fig. 3f, Sm/Gd ratios in all the zircon populations show infinitesimal variation defining a fractionation trend consistent with zircon unaffected by alteration or mineralization processes. A similar pattern and behavior were reported by Gardiner et al. (2021) for the Zaaiplaats granites in Bushveld Complex, South Africa. Thus, BAG zircons may have formed from REE-enriched melt that undergone fractionation. The wider variability in Eu anomalies across zircon populations from Bakoshi, Jaulere, Shanono, and Yettiti granites (Table S2) attest to their association with fractionated melt. However, the Hf contents of < 15,000 in the BAG granite zircons (except spots D1-1–9 and D2-1–3) imply that they were not highly fractionated (Grimes et al. 2015).

For a fractionated melt that crystallizes the BAG zircons, accessory phases, e.g., titanite, amphibole, ilmenite, and apatite, impact the ratios of U, Th, REE, Sc, and Nb (Grimes et al. 2015). The binary diagrams in Fig. 4 show a dominance of titanite and apatite fractionation during the melt of Bakoshi, Jaulere, Shanono, and Yettiti granites. Although zircons from these rocks appear to have amphibole in their system (Fig. 4c), its fractionation is negligible (Fig. 4d). Melt responsible for Gadanya alkali granite may not have experienced similar fractionation as the rest of BAG granite zircons mentioned above. Its zircons formed from cooling melt resulting from decreasing Gd/Yb and increasing Ce/Yb ratios (Fig. 4b). The similar trend displayed by the zircons (Gadanya granite inclusive; Fig. 4a)

imply crystal-chemical effect rather than fractionation of titanite and apatite because decreasing crystallization temperature favor incorporation of HREE over light and middle REE due to a crystal-chemical control on the REE substitution (Rubatto and Hermann 2007; Grimes et al. 2015). This is consistent with their HREE-enrichment patterns seen in Fig. 2.

## 5.2 Zircon elemental constrain on rock type and melt source

Zircon has proven a good candidate in Petrogenetic modelling (Watson and Harrison 1983; Bea 1996; Belousova et al. 2002; Corfu et al. 2003) due to its omnipresence in almost all rock types. Several trace elements (Y, Th, U, Nb, and Ta) and REE have provided excellent results in discriminating rock source and crystallization environment (e.g. Heaman et al. 1990; Belousova et al. 2002; Grimes et al. 2007). As highlighted in Sect. 5.1, the BAG zircons suffered no post crystallization alteration; thus, they can safely be used to trace the melt source of the high-K granites of the BAG area. Previous researches use REE patterns in deciphering magma source signature of igneous rocks but with no convincing results due to the overlapping nature of REE patterns in rocks from different source reservoirs (Grimes et al. 2007). This limits its emphasis herein. The discrimination diagrams in Figs. 7a–b (Belousova et al. 2002) pined the BAG granites to the granitoids field. Zircons from Gadanya alkali granite reside majorly in field 2, defined for granites on the Y versus Yb/Sm (and Nb/Ta) diagrams in Fig. 7. However, zircons from the rest of BAG granites occupied the field defined for aplites and leucogranites (field 1), granodiorite, and tonalities (field 3).

Since some zircon populations from the Bakoshi granite samples show a high U/Yb ratio imply crustal input in their melt. Classification of these rocks using whole-rock geochemical data by Elatikpo et al. (2021) has placed them as alkali granite and syenogranites. Thus, their position in the field broadly assigned to granitoids represent granites. Zircons are known for their high proclivity for U, Yb, and other heavy REE with ratios such as U/Yb in zircon considered to mirror the U/Yb ratio of the melt during its formation (Grimes et al. 2007). Applying the Hf contents and U/Yb ratios of study zircons in the diagram of Grimes et al. (2007), the zircons plot in the field of continental crust zircons derived from an enriched mantle source (Fig. 7c). The Plot of the U-Nb and U-Sc system (Figs. 7e–f; Grimes et al. 2015) alluded to this interpretation as most zircons plotted in the fields that overlapped OI-type (asthenospheric mantle-derive) and continental arc-type zircons, implying their formation in the active continental margin. Zircons from Gadanya alkali granite are restricted

to an OI-type field (Fig. 7e). A similar enriched lithospheric mantle source signature with crustal contamination was reported by Elatikpo et al. (2021) using integrated whole-rock Sr–Nd and zircon-Hf isotopic studies for these high-K granites.

Titanite and apatite fractionation may in part be responsible for the elevated U/Yb ratios that push much of the zircons close to the continental field; the parallelism of most zircons to mantle zircon array (Fig. 7e) is due to zircon crystallization in addition to withdrawal of phase such as apatite thus elevating the Nb/Yb and U/Yb ratios of the melt (Grimes et al. 2015). The conclusion is that most BAG granites derived their source from an enriched mantle metasomatized during the subduction process before its melting.

### 5.3 Magma temperature

Recent research by Elatikpo et al. (2021) documents the thermal evolution of the BAG granites using zircon saturation temperature (TZr). These authors identified two thermal regimes responsible for the formation of the BAG granites. First are the high temperatures with high Zr concentration granites (e.g. Shanono granite, Jaulere granite, Yettiti granite, and Gadanya alkali granite); the second category is the Bakoshi porphyritic granite. The presence of xenocrystic (inherited) zircons in some phases, e.g. Jaulere and Yettiti granites, led the authors not to conclude without asserting that the high temperature may be an over-estimation.

In this present study, we excluded xenocrystic zircon populations to ascertain the actual magma temperature during the crystallization of the granitic phases, and two thermal regimes were also identified (Fig. 6a). Bakoshi granite samples D1-1, Yettiti granite, and Gadanya alkali granite defined the line of the lower thermal boundary with a mean temperature range of 705–653 °C. Those with high mean temperatures are the Shanono granite, Jaulere granite, and Bakoshi granite sample D2-1 (mean = 746–724°C). The thermal boundaries established here are not at variance with the TZr temperature given by Elatikpo et al. (2021). All the BAG zircons except for sample D2-1 have a mean temperature close/and or comparable to the TZr temperature of Elatikpo et al. In Figs. 5a and 5e, and Table S1-1 shows much temperature variation and Ti content compared to rest samples, possibly resulting from the ablation of unavoidable Ti-rich inclusions at micro to nanoscales not detected in CL and reflected light images during laser spot selection. The higher temperature in Bakoshi sample D2-1 is consistent with its early formation age (646 Ma) compared to the younger Bakoshi D1-1 formed at 638 Ma. Ti-in-Zircon temperature range of 797–624 °C for Gadanya alkali granite is within its TZr (853 – 683 °C, mean

768 °C), though it has a mean value of 705 °C lower than its reported mean TZr of 768 °C. This may be connected to its silica oversaturated melt (76–77 wt.%; Elatikpo et al. 2021). This is ideal because titanium concentration decreases as melt gets saturated in silica (Fu et al. 2008). The relatively lower than 608 °C temperatures recorded in a few zircons from some granitic samples (D1-1, D2-1, J1-1, and Y2-1) may be their formation below the saturation temperature at specific ranges. In their experimental work on Ti-in-Zircon temperature, Fu et al. (2008) reported the same phenomenon.

### 5.4 Magmas redox state

Multiple valence states of some REE, e.g., europium and cerium, allow their incorporation into zircon structure at different redox conditions (Trail et al. 2012). The preference of zircon in partitioning Ce<sup>4+</sup> over Ce<sup>3+</sup> makes it easy to apply the Ce<sup>4+</sup>/Ce<sup>3+</sup> ratio to determine the magma oxygen fugacity (Zhang et al. 2020; Ballard et al. 2002). Of all the trace elements, rare earth elements are more promising in petrogenetic modelling, especially where there is a coexistence of phases such as xenotime, monazite, allanite, or apatite (Hoskin and Ireland 2000; Poirier et al. 2002). Positive or negative Ce anomalies imply that the zircon was formed in a high or low oxidation environment, respectively, which is usually accompanied by high oxygen fugacity as in the case of positive Ce anomaly or low oxygen fugacity if it is a negative Ce anomaly (Ballard et al. 2002).

The equation of computing Ce<sup>+4</sup>/Ce<sup>+3</sup> values using the lattice-strain model developed by Ballard et al. (2002) is the most adopted method in determining oxy-barometer. However, recent studies have identified this method's pitfall due to the repelling nature of zircon on La and Pr (the LREE), thus giving a false analysis by underestimation (Corfu et al. 2003; Hoskin and Schaltegger 2003; Jiang et al. 2020). A software-based method (Geo-fO<sub>2</sub>) developed by Li et al. (2019) depends on Nd, Sm, and HREE as against the use of LREE to determine the oxygen fugacity is thus more convenient and is adopted in the estimation of the Ce<sup>+4</sup>/Ce<sup>+3</sup>, fO<sub>2</sub>, and other parameters contained in Table S2.

Magma that crystallized the Gadanya alkali granite is constrained to have evolved under oxidizing conditions (Table S2; Fig. 8a). These were evident through combined Ce- and Eu-anomalies, in addition to Ce<sup>4+</sup>/Ce<sup>3+</sup> ratios of zircons from Gadanya alkali granite. In addition, the plot of logfO<sub>2</sub> versus Temperatures (Fig. 8a) placed Gadanya alkali granite above the haematite-magnetite buffer (mean ΔFMQ + 9.5), thus, far beyond the FMQ boundary defined for an oxidized granite. Similarly, Jaulere biotite granite plots above FMQ buffer (mean ΔFMQ + 1.6). However,

zircon grains from the rest of BAG granites: Bakoshi granite, Shanono granite, and Yettiti granite resided below the FMQ buffer but above the boundary defined for  $\text{CO}_2$  and graphite buffer. Compared to Gadanya alkali granite, they have lower  $\text{Ce}^{4+}/\text{Ce}^{3+}$  ratios and Eu anomalies which constrained them to reduced granites formed under reducing magma conditions. However, countable zircon fractions from Shanono granite mingled with the oxidized zircons above the FMQ line (Fig. 8a).

### 5.5 Likely implication of magma redox state on the associated gold mineralization

Magmatic source fluids are responsible in some instances for the precipitation of gold metal through exsolution of gold from sulfides melt and through crystallization of an oxidizing mineral such as magnetite under favorable physicochemical conditions (Simon et al. 2003). Asaah et al. (2015) and Sun et al. (2004, 2013) have shown that an oxidized melt can house a significant concentration of gold, after which precipitation of oxidizing minerals such as magnetite and hematite is capable of altering the redox state of the melt through  $\text{Fe}^{+3}$ , thereby reducing sulfate to sulfide ( $\text{SO}_4^{-2}$  to  $\text{S}^{-2}$ ) and the formation of Au hydrosulfide [ $\text{Au}(\text{HS})^0$  or  $\text{Au}(\text{HS})_2^-$ ].

Zircons from the BAG granitic rocks displayed characteristics of both oxidized and reduced granites. As shown in Sect. 5.4, zircons from Gadanya alkali granite, and to some extent, the Jaulere biotite granite show a proclivity for oxidized granites and plotted above the Fayalite-Magnetite-Quartz buffer (Fig. 8a). The attainment of haematite-magnetite oxygen buffer by Gadanya granite zircon populations makes it favorable for copper mineralization (Sun et al. 2013). However, the pH values must be near or excess of neutral value.

By applying  $\text{Ce}^{4+}/\text{Ce}^{3+}$  ratios versus  $\text{Eu}/\text{Eu}^*$  in a binary diagram (Fig. 8b) (e.g. Zhang et al. 2020), only Gadanya alkali granite indicates the potential to be associated with  $\text{Cu} \pm \text{Au}$  ore-bearing granites due to its higher  $\text{Ce}^{4+}/\text{Ce}^{3+}$  values ( $> 100$ , mean 1485) relative to the rest BAG granites; an indication of the high chemical potential of the oxygen from an oxidized magma source. The Jaulere biotite granite, however, shows low  $\text{Ce}^{4+}/\text{Ce}^{3+}$  values (mostly  $< 100$ , mean 39) within the range for barren granites from Los Picos-Fortuna/Pajonal-El Abra Complex of northern Chile (Fig. 8b). Thus, Gadanya alkali granite may have formed from a more oxidizing magma compared with the rest of BAG granites and is comparable to oxidized and ore-bearing granites from Dexing in China (Zhang et al. 2020), Chuquicamata-El Abra porphyry copper belt in Chile (Ballard et al. 2002) and the molybdenum-bearing granite from Mada Complex in Nigeria (Girei et al. 2020) (Fig. 8b). Previous researches (e.g.

Kemp 2005; Zhang et al. 2020; Girei et al. 2020) associated oxidized granites with high oxygen fugacity and  $\text{Ce}^{4+}/\text{Ce}^{3+}$  ratios such as the Gadanya alkali granite to copper, gold, and molybdenum mineralization. The range of  $\log/\text{O}_2$  for zircons from Gadanya alkali granite is within the  $-18$  to  $-11$  reported for copper arc samples in Myanmar (Gardiner et al. 2017) noted for their  $\text{Cu} \pm \text{Au}$  potential; likewise, the Hf content and U/Yb ratios of zircons from this granite plots in the fields of Cu and Mo bearing granites for Myanmar and Mada Complex in Nigeria, respectively (Fig. 8c).

On the other hand, Bakoshi porphyritic granites, Shanono granite, and Yettiti medium-grained granite plots in reduced granites field (Blevin et al. 1996; Ishihara 1977). Some reduced granites are known for their potential for economic concentration of tin, tungsten, and even tantalum mineralization (Kemp 2005; Gardiner et al. 2021; Wu et al. 2021; Zhao et al. 2022). The ranges of  $\log/\text{O}_2$  for the BAG reduced granites are within the calculated  $-34$  to  $-19$  for the tin belt in Myanmar (Gardiner et al. 2017). In addition, Bakoshi granite samples reside well in the field defined for the tin belt in Myanmar (Fig. 8c). However, there is no report of tin occurrence in the BAG area, which may in part be non-discovery by artisanal miners, as has been the case in Nigeria.

Other workers (e.g. Müller and Groves 2019 and references therein) have asserted that the potential of high-k igneous rocks of the suitability of Au-Cu mineralization can also be investigated through the halogen (e.g. Cl and F) content of the mica phenocrysts in this rock type. They considered the Cl and F content greater than 0.04 and 0.5 wt.%, respectively, a good prospect for these metals (Müller et al. 2001; Sarjoughian et al. 2015). Although, during this investigation, we did not test for the halogen content of any mica mineral to ascertain the suitability or association of the BAG granites, as shown by the magmas' determined redox state. Future work on the halogen contents of these granites will help elucidate this.

In summary, granitic rocks of the BAG area may have either the genetic affiliation or mere hosting capability of the gold mineralization (e.g. Gadanya alkali granite) or potential for tin mineralization (the reduced type: Bakoshi granite) (e.g. Guo et al. 2020; Zhang et al. 2020). However, isotope systematics and geochronology of the gold deposit of the BAG area would be needed to constrain the genetic link of the BAG granites.

## 6 Conclusions

Zircons from the Bakoshi-Gadanya granites defined two probable metallogenetic source granites: 1) high  $\text{Ce}^{4+}/\text{Ce}^{3+}$  ratio with high oxygen fugacity granite such as the

Gadanya alkali granite may probably have a proclivity with the gold mineralization in the study area, and 2) the reduced granites including Bakoshi porphyritic granite, Shanono coarse-grained granite, and Yettiti medium-grained granite, characterized by their moderate to low  $\text{Ce}^{4+}/\text{Ce}^{3+}$  ratios and oxygen fugacity, exclude them as potential source candidates for the associated BAG gold mineralization. However, Bakoshi reduced granite may likely have the potential for either Sn or Ta mineralization as it has zircon chemistry comparable to zircons from the tin belt in Myanmar. Zircon trace elements fingerprint the source of the reduced high-K BAG granites to an enriched mantle lithosphere. In contrast, the oxidized melt that crystallized into Gadanya alkali granite derives from the asthenospheric mantle (OI-type).

**Supplementary Information** The online version contains supplementary material available at <https://doi.org/10.1007/s11631-022-00528-z>.

**Acknowledgements** This work was co-financed by the National Natural Science Foundation of China (Grant No. 41502067) and the Science and Technology Innovation Program of Hunan Province (Grant No. 2021RC4055). Comments and suggestions by two anonymous reviewers helped improved the manuscript and are acknowledged. We'd like to thank Dr. Wang for his editorial handling.

## Declaration

**Conflict of interests** No potential conflict of interest was reported by the author(s).

## References

- Adetunji A, Olarewaju VO, Ocan OO, Macheva L, Ganev VY (2018) Geochemistry and U-Pb zircon geochronology of Iwo quartz potassic syenite, southwestern Nigeria: constraints on petrogenesis, timing of deformation and terrane amalgamation. *Precam Res* 307:125–136. <https://doi.org/10.1016/j.precamres.2018.01.015>
- Ajibade AC, Wright JB (1989) The Togo-Benin-Nigeria shield: evidence of crustal aggregation in the Pan-African belt. *Tectonophysics* 165(1–4):125–129. [https://doi.org/10.1016/0040-1951\(89\)90041-3](https://doi.org/10.1016/0040-1951(89)90041-3)
- Ananaba SE, Ajakaiye DE (1987) Evidence of tectonic control of mineralization in Nigeria from lineament density analysis a landsat-study. *Int J Remote Sens* 8:1445–1453. <https://doi.org/10.1080/01431168708954788>
- Anders E, Grevesse N (1989) Abundances of the elements: meteoritic and solar. *Geochim Cosmochim Acta* 53(1):197–214. [https://doi.org/10.1016/0016-7037\(89\)90286-X](https://doi.org/10.1016/0016-7037(89)90286-X)
- Anthony AM, Abubakar-Zaria U, Atta AY, Magaji SS (2020) Recovery of gold from Shanono gold ore deposit using  $\alpha$ -cyclodextrin. *Min Metall Explor* 37:1265–1271. <https://doi.org/10.1007/s42461-020-00227-4>
- Asaah AV, Zoheir B, Lehmann B, Frei D, Suh CE, Victor A, Zoheir B, Lehmann B, Frei D (2015) Geochemistry and geochronology of the ~620 Ma gold-associated Batouri granitoids, Cameroon. *Inter Geol Rev* 57:1485–1509. <https://doi.org/10.1080/00206814.2014.951003>
- Ballard JR, Palin JM, Campbell IH (2002) Relative oxidation states of magmas inferred from Ce“IV”/Ce“III” in zircon: Application to porphyry copper deposits of northern Chile. *Contrib Mineral Petro* 144:347–364. <https://doi.org/10.1007/s00410-002-0402-5>
- Bea F (1996) Residence of REE, Y5 Th and U in granites and crustal protoliths; implications for the chemistry of crustal melts. *J Petro* 37(3):521–552. <https://doi.org/10.1093/petrology/37.3.521>
- Belousova E, Griffin W, O'Reilly SY, Fisher N (2002) Igneous zircon: trace element composition as an indicator of source rock type. *Contrib Mineral Petro* 143:602–622. <https://doi.org/10.1007/s00410-002-0364-7>
- Béchir-Benmerzoug F, Azzouni-Sekkal A, Liégeois JP, Bonin B, Bechiri H, Kheloui R (2018) The Silet superterrane (Western Hoggar, Algeria): A collage of exotic terranes. In: 27th Colloquium of African Geology, Aveiro, Portugal, July 2018
- Béchir-Benmerzoug F, Liégeois JP, Bonin B, Azzouni-Sekkal A, Bechiri H, Kheloui R, Matukov DI, Sergeev SA (2011) The plutons from the Cryogenian Iskel composite oceanic island arc (Hoggar, Tuareg Shield, Algeria): U-Pb on zircon SHRIMP geochronology, geochemistry and geodynamic setting. In: Seventh Hutton symposium on granites and related rocks, Avila, Spain, July 4–9, p 17
- Blevin PL, Chappell BW (1995) Chemistry, origin, and evolution of mineralized granites in the Lachlan Fold Belt, Australia: the metallogeny of I- and S-type granites. *Econ Geol* 90:1604–1619. <https://doi.org/10.2113/gsecongeo.90.6.1604>
- Blevin PL, Chappell BW (1992) The role of magma sources, oxidation states and fractionation in determining the granite metallogeny of eastern Australia. *Trans R Soc Edinb Earth Sci* 83(1–2):305–316. <https://doi.org/10.1017/S0263593300007987>
- Blevin PL, Chappell B, Allen C (1996) Intrusive metallogenic provinces in eastern Australia based on granite source and composition. *Trans R Soc Edinb Earth Sci* 87:281–290. <https://doi.org/10.1017/s0263593300006684>
- Boehnke P, Watson EB, Trail D, Harrison TM, Schmitt AK (2013) Zircon saturation re-revisited. *Chem Geol* 351:324–334. <https://doi.org/10.1016/j.chemgeo.2013.05.028>
- Bouvier AS, Ushikubo T, Kita NT, Cavosie AJ, Kozdon R, Valley JW (2011) Li isotopes and trace elements as a petrogenetic tracer in zircon: insights from Archean TTGs and sanukitoids. *Contrib Mineral Petro* 163:745–768. <https://doi.org/10.1007/s00410-011-0697-1>
- Brahimi S, Liégeois JP, Ghienne JF, Munsch M, Bourmatte A (2018) The Tuareg shield terranes revisited and extended towards the northern Gondwana margin: magnetic and gravimetric constraints. *Earth-Sci Rev* 185:572–599. <https://doi.org/10.1016/j.earscirev.2018.07.002>
- Bruguer O, Data S, Lancelot JR (1994) Early Archaean component (> 3.5 Ga) within a 3.05 Ga orthogneiss from northern Nigeria: UPb zircon evidence. *Earth Planet Sci Lett* 125(1–4):89–103. [https://doi.org/10.1016/0012-821X\(94\)90208-9](https://doi.org/10.1016/0012-821X(94)90208-9)
- Bute SI, Yang X, Suh CE, Girei MB, Usman MB (2020a) Mineralogy, geochemistry and ore genesis of Kanawa uranium mineralization, Hawal Massif, eastern Nigeria terrane: Implications for uranium prospecting in Nigeria and Cameroon. *Ore Geol Rev* 120:103381. <https://doi.org/10.1016/j.oregeorev.2020.103381>
- Bute SI, Yang X, Cao J, Liu L, Deng J, Vela Haruna I, Girei MB, Abubakar U, Akhtar S (2020b) Origin and tectonic implications of ferroan alkali-calcic granitoids from the Hawal Massif, east-eastern Nigeria terrane: Clues from geochemistry and zircon U-Pb-Hf isotopes. *Int Geol Rev* 62(2):129–152. <https://doi.org/10.1080/00206814.2019.1593250>

- Caby R (2003) Terrane assembly and geodynamic evolution of central-western Hoggar: a synthesis. *J Afri Earth Sci* 37(3–4):133–159. <https://doi.org/10.1016/j.jafrearsci.2003.05.003>
- Chappell BW, White AJR (2001) Two contrasting granite types: 25 years later. *Aust J Earth Sci* 48(4):489–499. <https://doi.org/10.1046/j.1440-0952.2001.00882.x>
- Cheng Y, Spandler C, Chang Z, Clarke G (2018) Volcanic–plutonic connections and metal fertility of highly evolved magma systems. A case study from the Herberton Sn–W–Mo Mineral Field, Queensland, Australia. *Earth Planet Sci Lett* 486:84–93. <https://doi.org/10.1016/j.epsl.2018.01.012>
- Corfu F, Hanchar JM, Hoskin PWO, Kinniy P (2003) Atlas of zircon textures. *Rev Mineral Geochem* 53(1):469–500. <https://doi.org/10.2113/0530469>
- Dada SS (1998) Crust-forming ages and proterozoic crustal evolution in Nigeria: A reappraisal of current interpretations. *Precambrian Res* 87:65–74. [https://doi.org/10.1016/s0301-9268\(97\)00054-5](https://doi.org/10.1016/s0301-9268(97)00054-5)
- Dada SS, Lancelot JR, Briqueu L (1989) Age and origin of the annular charnockitic complex at Toro, Northern Nigeria: U-Pb and Rb-Sr evidence. *J Afri Earth Sci* 9(2):227–234. [https://doi.org/10.1016/0899-5362\(89\)90066-3](https://doi.org/10.1016/0899-5362(89)90066-3)
- Danbatta UA (1999) The geotectonic evolution of the Kazaure Schist belt in the Precambrian Basement of NW Nigeria. Ph.D thesis, Ahmadu Bello University Zaria 298 p
- De Wit MJ, Stankiewicz J, Reeves C (2008) Restoring pan-African–Brasiliano connections: more Gondwana control, less Trans-Atlantic corruption. *Geol Soc Lond Spec Pub* 294(1):399–412. <https://doi.org/10.1144/SP294.20>
- Elatikpo SM, Li H, Zheng H, Girei MB, Wu J, Amuda AK (2021) Cryogenian crustal evolution in western Nigeria shield: whole-rock geochemistry, Sr-Nd, and zircon U-Pb-Hf isotopic evidence from Bakoshi–Gadanya granites. *Int Geol Rev*. <https://doi.org/10.1080/00206814.2021.1998799>
- Elatikpo SM, Girei MB, Adamu MS (2018) The Crude Techniques of Gold Recovery: A Study of Alajawa Kundila Artisanal Gold Mine, Nigeria. In: 54th annual international conference and exhibition of the Nigerian mining and geosciences society (NMGS), Kano, Nigeria, March 18–23, abstract p 141
- Elatikpo SM (2016) Style of Gold mineralization in the Pan-African terrain of Nigeria: a review. Ahmadu Bello University Zaria, A seminar paper presented at the Department of Geology, 19p
- Ferré EC, Déléris J, Bouchez JL, Lar AU, Peucat JJ (1996) The Pan-African reactivation of Eburnean and Archaean provinces in Nigeria: structural and isotopic data. *J Geol Soc Lond* 153(5):719–728. <https://doi.org/10.1144/gsjgs.153.5.0719>
- Fu B, Page BZ, Cavosie AJ, Fournelle J, Kita NT, Lackey JS, Wilde SA, Valley JW (2008) Ti-in-zircon thermometry: applications and limitations. *Contrib Mineral Petrol* 156:197–213. <https://doi.org/10.1007/s00410-008-0281-5>
- Gardiner NJ, Hawkesworth CJ, Robb LJ, Mulder JA, Wainwright AN, Cawood PA (2021) Metal anomalies in zircon as a record of granite-hosted mineralization. *Chem Geol* 585:120580. <https://doi.org/10.1016/j.chemgeo.2021.120580>
- Gardiner NJ, Hawkesworth CJ, Robb LJ, Whitehouse MJ, Roberts NMW, Kirkland CL, Evans NJ (2017) Contrasting granite metallogeny through the Zircon record: a case study from Myanmar. *Sci Rep* 7:1–8. <https://doi.org/10.1038/s41598-017-00832-2>
- Girei MB, Li H, Vincent VI, Algeo TJ, Elatikpo SM, Bute SI, Ahmed HA, Amuda AK (2020) Genesis and timing of Mo mineralization in the Mada Ring Complex, north-central Nigeria: insights from whole-rock geochemistry, Nd-Sr isotopes, zircon U-Pb-Hf isotopes, and molybdenite Re-Os systematics. *Miner Depos*. <https://doi.org/10.1007/s00126-020-01019-y>
- Goodenough KM, Lusty PAJ, Roberts NMW, Key RM, Garba A (2014) Post-collisional Pan-African granitoids and rare metal pegmatites in western Nigeria: age, petrogenesis, and the ‘pegmatite conundrum.’ *Lithos* 200–201:22–34. <https://doi.org/10.1016/j.lithos.2014.04.006>
- Grimes CB, Wooden JL, Cheadle MJ, John BE (2015) “Fingerprinting” tectono-magmatic provenance using trace elements in igneous zircon. *Contrib Mineral Petrol* 170(46):1–26. <https://doi.org/10.1007/s00410-015-1199-3>
- Grimes CB, John BE, Kelemen PB, Mazdab FK, Wooden JL, Cheadle MJ, Schwartz JJ (2007) Trace element chemistry of zircons from oceanic crust: a method for distinguishing detrital zircon provenance. *Geology* 35(7):643–646. <https://doi.org/10.1130/G23603A.1>
- Guo H, Lai Y, Zhou Y, Lv X (2020) The role of magma sources, oxygen fugacity, and fractionation in determining the Jiudingshan porphyry-skarn Cu–Mo deposit in Western Yunnan, China. *Geol J*. <https://doi.org/10.1002/gj.3885>
- Harrison TM, Blachert-Toft J, Müller W, Albarede F, Holden P, Mojzsis SJ, (2005) Heterogeneous Hadean hafnium: evidence of continental crust at 4.4 to 4.5 Ga. *Science* 310:1947–1950. <https://doi.org/10.1126/science.1117926>
- Heaman LM, Bowins R, Crocket J (1990) The chemical composition of igneous zircon suites: implications for geochemical tracer studies. *Geochim Cosmochim Acta* 54(6):1597–1607. [https://doi.org/10.1016/0016-7037\(90\)90394-Z](https://doi.org/10.1016/0016-7037(90)90394-Z)
- Hoskin PWO, Schaltegger U (2003) The composition of zircon and igneous and metamorphic petrogenesis. *Rev Mineral Geochem* 53:27–62. <https://doi.org/10.2113/0530027>
- Hoskin PWO, Ireland TR (2000) Rare earth element chemistry of zircon and its use as a provenance indicator. *Geology* 28(7):627–630. [https://doi.org/10.1130/0091-7613\(2000\)28%3c627:RECOZ%3e2.0.CO;2](https://doi.org/10.1130/0091-7613(2000)28%3c627:RECOZ%3e2.0.CO;2)
- Ishihara S (1977) The magnetite-series and ilmenite-series granitic rocks. *Mining Geol* 27(145):293–305. <https://doi.org/10.11456/shigenchishitsu1951.27.293>
- Jiang WC, Li H, Turner S, Zhu DP, Wang C (2020) Timing and origin of multi-stage magmatism and related W–Mo–Pb–Zn–Fe–Cu mineralization in the Huangshaping deposit, South China: an integrated zircon study. *Chem Geol* 552:119782. <https://doi.org/10.1016/j.chemgeo.2020.119782>
- Jiang WC, Li H, Evans NJ, Wu JH (2019) Zircon records multiple magmatic-hydrothermal processes at the giant Shizhuyuan W–Sn–Mo–Bi polymetallic deposit, South China. *Ore Geol Rev* 115:103160. <https://doi.org/10.1016/j.oregeorev.2019.103160>
- Kemp AIS, Wilde SA, Hawkesworth CJ, Coath CD, Nemchin A, Pidgeon RT, Vervoort JD, DuFrane SA (2010) Hadean crustal evolution revisited: new constraints from Pb–Hf isotope systematics of the Jack Hills zircons. *Earth Planet Sci Lett* 296:45–56. <https://doi.org/10.1016/j.epsl.2010.04.043>
- Kemp AIS (2005) Granite. In: Selley RC, Cocks LRM, Plimer IR (eds) *Encyclopedia of Geol*. Elsevier, pp 233–247
- Krneta S, Ciobanu CL, Cook NJ, Ehrig K, Kontonikas-Charos A (2017) Rare earth element behaviour in apatite from the olympic dam Cu–U–Au–Ag deposit, South Australia. *Minerals* 7(8):135. <https://doi.org/10.3390/min7080135>
- Kröner A, Ekwueme BN, Pidgeon RT (2001) The oldest rock in West Africa: SHRIMP zircon age for early Archean migmatitic orthogneiss at Kaduna, Northern Nigeria. *J Geol* 109(3):399–406. <https://doi.org/10.1086/319979>
- Lee RG, Byrne K, D’Angelo M, Hart CJR, Hollings P, Gleeson SA, Alfaro M (2021) Using zircon trace element composition to assess porphyry copper potential of the Guichon Creek batholith and Highland Valley copper deposit, south-central British

- Columbia. Miner Depos 56:215–238. <https://doi.org/10.1007/s00126-020-00961-1>
- Li W, Cheng Y, Yang Z (2019) Geo- $f\text{O}_2$ : integrated software for analysis of magmatic oxygen fugacity. *Geochem Geophys Geosyst* 20:2542–2555. <https://doi.org/10.1029/2019GC008273>
- Liégeois JP (2019) A new synthetic geological map of the Tuareg Shield: an overview of its global structure and geological evolution. In: Bendaoud A, Hamimi Z, Hamoudi M, Djemai S, Zoheir B (eds) *The Geology of the Arab World - An overview*. Springer Geology, Cham, pp 83–107. <https://doi.org/10.1007/978-3-319-96794-3>
- Linch RJ, Hanchar JM (2003) Structure and chemistry of zircon and zircon-group minerals. *Rev Mineral Geochem* 53(1):1–25. <https://doi.org/10.2113/0530001>
- Liu YS, Gao S, Kelemen PB, Xu W (2008) Recycled crust controls contrasting source compositions of Mesozoic and Cenozoic basalts in the North China Craton. *Geochim Cosmochim Acta* 72:2349–2376. <https://doi.org/10.1016/j.gca.2008.02.018>
- Müller D, Franz L, Herzig PM, Hunt S (2001) Potassic igneous rocks from the vicinity of epithermal gold mineralization, Lihir Island, Papua New Guinea. *Lithos* 57:163–186. [https://doi.org/10.1016/S0024-4937\(01\)00035-4](https://doi.org/10.1016/S0024-4937(01)00035-4)
- Müller D, Groves DI (2019) Tectonic settings of potassic igneous rocks. In: *Potassic igneous rocks and associated gold-copper mineralization*. Mineral Res Rev. Springer, Cham. [https://doi.org/10.1007/978-3-319-92979-8\\_3](https://doi.org/10.1007/978-3-319-92979-8_3)
- Ogezi AE (1977) *Geochemistry and geochronology of basement rocks from northwestern Nigeria*. Ph.D thesis University of Leeds, England
- Ouattara Z, Coulibaly Y, Boiron MC (2020) Intrusion-related gold systems in Côte d'Ivoire; the Bonikro Au deposit story. *Ore Deposits Hub presentation*, October 7, 2020. <https://www.youtube.com/watch?v=8OeiID86NEo>
- Poitrasson F, Hanchar JM, Schaltegger U (2002) The current state and future of accessory mineral research. *Chem Geol* 191(1–3):3–24. [https://doi.org/10.1016/S0009-2541\(02\)00146-8](https://doi.org/10.1016/S0009-2541(02)00146-8)
- Rubatto D, Hermann J (2007) Experimental zircon/melt and zircon/garnet trace element partitioning and implication for the geochronology of crustal rocks. *Chem Geol* 241:38–61. <https://doi.org/10.1016/j.chemgeo.2007.01.027>
- Sani MA, Raimi J, Elatikpo SM, Lawal KM (2017) Magnetic interpretation of structures associated with Gold mineralisation Around Kundila and Ginzo area, Northwestern Nigeria Nigerian. *J Sci Res* 16(2):240–246
- Sarjoughian F, Kananian A, Ahmadian J, Murata M (2015) Chemical composition of biotite from the Kuh-e Dom pluton, Central Iran: implication for granitoid magmatism and related Cu–Au mineralization. *Arab J Geosci* 8:1521–1533. <https://doi.org/10.1007/s12517-013-1242-5>
- Schaltegger U (2007) Hydrothermal zircon. *Elements* 3(1):51–79. <https://doi.org/10.2113/gselements.3.1.51>
- Simon AC, Pettke T, Candela PA, Piccoli PM, Heinrich CA (2003) Experimental determination of Au solubility in rhyolite melt and magnetite: constraints on magmatic Au budgets. *Am Mineral* 88(11–12):1644–1651. <https://doi.org/10.2138/am-2003-11-1202>
- Smythe DJ, Brenan JM (2016) Magmatic oxygen fugacity estimated using zircon-melt partitioning of cerium. *Earth Planet Sci Lett* 453:260–266. <https://doi.org/10.1016/j.epsl.2016.08.013>
- Sun SS, McDonough WF (1989) Chemical and isotopic systematics of oceanic basalts: implications for mantle composition and processes. *Geol Soc Spec Publ* 42:313–345. <https://doi.org/10.1144/GSL.SP.1989.042.01.19>
- Sun W, Liang H, Ling MX, Zhan M, Ding X, Zhang H, Yang XY, Li Y, Ireland T, Wei Q, Fan W (2013) The link between reduced porphyry copper deposits and oxidized magmas. *Geochim Cosmochim Acta* 103:263–275. <https://doi.org/10.1016/j.gca.2012.10.054>
- Sun W, Arculus RJ, Kamenetsky VS, Binns RA (2004) Release of gold-bearing fluids in convergence margin magmas prompted by magnetite crystallization. *Nature* 431:975–978. <https://doi.org/10.1038/nature02972>
- Trail D, Bruce WE, Tailby ND (2012) Ce and Eu anomalies in zircon as proxies for the oxidation state of magmas. *Geochim Cosmochim Acta* 97:70–87. <https://doi.org/10.1016/j.gca.2012.08.032>
- Watson EB, Wark DA, Thomas JB (2006) Crystallization thermometers for zircon and rutile. *Contrib Mineral Petrol* 151:413–433. <https://doi.org/10.1007/s00410-006-0068-5>
- Watson EB, Harrison TM (1983) Zircon saturation revisited: temperature and composition effects in a variety of crustal magma types. *Earth Planet Sci Lett* 64(2):295–304. [https://doi.org/10.1016/0012-821X\(83\)90211-X](https://doi.org/10.1016/0012-821X(83)90211-X)
- Woakes M, Rahaman MA, Ajibade AC (1987) Some metallogenetic features of the Nigerian basement. *J Afric Earth Sci* 6:655–664. [https://doi.org/10.1016/0899-5362\(87\)90004-2](https://doi.org/10.1016/0899-5362(87)90004-2)
- Wu J, Kong H, Li H, Algeo TJ, Yonezu K, Liu B, Wu Q, Zhu D, Jiang H (2021) Multiple metal sources of coupled Cu–Sn deposits: Insights from the Tongshanling polymetallic deposit in the Nanling Range, South China. *Ore Geol Rev* 139:104521. <https://doi.org/10.1016/j.oregeorev.2021.104521>
- Zhang Z, Ling M, Zhang L, Sun S, Sun W (2020) High oxygen fugacity magma: implication for the destruction of the North China Craton. *Acta Geochim* 39:161–171. <https://doi.org/10.1007/s11631-020-00394-7>
- Zhao P, Zajacz Z, Tsay A, Yuan S (2022) Magmatic-hydrothermal tin deposits form in response to efficient tin extraction upon magma degassing. *Geochim Cosmochim Acta* 316:331–346. <https://doi.org/10.1016/j.gca.2021.09.011>
- Zhong S, Feng C, Seltmann R, Li D, Qu H (2018) Can magmatic zircon be distinguished from hydrothermal zircon by trace element composition? The effect of mineral inclusions on zircon trace element composition. *Lithos* 314–315:646–657. <https://doi.org/10.1016/j.lithos.2018.06.029>